Improving Intergranular Stress Corrosion Cracking Resistance in a Fe–18Cr–17Mn–2Mo–0.85N Austenitic Stainless Steel Through Grain Boundary Character Distribution Optimization

F. Shi[1] · L. Yan[1] · J. Hu[1] · L. F. Wang[1] · T. Z. Li[1] · W. Li[1] · X. J. Guan[1] · C. M. Liu[3] · X. W. Li[1,2]

Abstract

The grain boundary character distribution (GBCD) optimization and its effect on the intergranular stress corrosion cracking (IGSCC) resistance in a cold-rolled and subsequently annealed Fe–18Cr–17Mn–2Mo–0.85N high-nitrogen nickel-free austenitic stainless steel were systematically explored. The results show that stacking faults and planar slip bands appearing at the right amount of deformation (lower than 10%) are beneficial cold-rolled microstructures to the GBCD optimization. The proportion of special boundaries gradually increases in the subsequent stages of recrystallization and grain growth, accompanying with the growth of twin-related domain in the experimental steel. In this way, the fraction of low Σ coincidence site lattice (CSL) boundaries can reach as high as 82.85% for the specimen cold-rolled by 5% and then annealed at 1423 K for 72 h. After GBCD optimization, low Σ CSL boundaries and the special triple junctions ($J2$, $J3$) of high proportion can greatly hinder the nitride precipitation along grain boundaries and enhance the capability for intergranular crack arrest, thus improving the IGSCC resistance of the experimental steel.

1 Introduction

Grain boundary character distribution (GBCD) optimization or grain boundary engineering (GBE) has been widely concerned as a new approach to solve the problem of grain boundary (GB) failure in recent years [1–5]. The main idea of GBE firstly proposed by Watanabe [6] originates from the concept of "GB design and control," namely, increasing the proportion of GBs with special properties (low Σ

✉ X. W. Li
  xwli@mail.neu.edu.cn

1 Department of Materials Physics and Chemistry, School of Materials Science and Engineering, Northeastern University, Shenyang 110819, China

2 State Key Laboratory of Rolling and Automation, Northeastern University, Shenyang 110819, China

3 Key Laboratory for Anisotropy and Texture of Materials (Ministry of Education), Northeastern University, Shenyang 110819, China

coincidence site lattice (CSL) boundaries) in GBCD will improve the overall performance of the alloy, especially the resistance to GB failure through thermo-mechanical process (TMP) in the face-centered cubic metal material with low stacking fault energy (SFE). GBE has proven to be effective in preventing intergranular corrosion (IGC) and intergranular stress corrosion cracking (IGSCC) caused by carbide precipitation in the traditional austenitic stainless steel (ASS) (e.g., 304 [7–9] and 316 [10–13] ASSs) and nickel-based alloys (e.g., 600 [14–18] and 690 [11, 19] alloys).

High-nitrogen nickel-free ASS is a new and advanced steel material, in which nickel is totally replaced by additions of manganese and nitrogen. The addition of nitrogen will not only improve the mechanical properties and local corrosion performance, but also significantly reduce the cost of the material [20–27]. However, a high nitrogen content may cause the precipitation of nitrides during welding in such advanced steels [28–30]. The nitride precipitation can cause a serious GB failure problem in the heat-affected zone, such as IGC, IGSCC and corrosion fatigue, which directly limits the practical applications of such advanced steel materials.

There are few studies on GBE improving the GB performance weakened by nitride in high-nitrogen steel [31–34]. Kokawa et al. [31] reported that the fraction of low Σ CSL boundaries can be raised to 87% in a Fe–23Cr–4Ni–2Mo–1N high-nitrogen ASS cold-rolled by 2% and then annealed at 1423 K for 48 h, and intergranular and cellular chromium nitride precipitation in the heat-affected zone was thus greatly inhibited in such a GBEed specimen compared with the solid solution-treated specimen. Their research findings [31] have suggested that the GBCD optimization suppressed the nitride precipitation in the heat-affected zone during welding, but concrete corrosion results were not given and the relevant mechanism of GBE for improving the IGC problem was not elaborated. Our previous work [32] reported that the proportion of special boundaries (SBs) reached 79.4% through an annealing treatment at 1423 K for 72 h after 5% cold-rolling deformation and the IGC resistance was significantly improved in an Fe–20Cr–19Mn–2Mo–0.82N high-nitrogen nickel-free ASS. According to the above few investigations on the GBE of high-nitrogen ASS, it can be realized that GBE should have a great potential in solving the problem of GB failure caused by the nitride precipitation in high-nitrogen ASS. Moreover, it is noticed that the GBCD optimization reported in the traditional ASS is mainly based on two types of heat treatments, i.e., annealing at a low temperature for a long time [8, 10] or annealing at a high temperature for a short time [1, 12]. However, different GBE processes were actually found in some high-nitrogen ASSs [31, 32]. Different processes correspond surely to different GBCD optimization mechanisms. The present work focuses on the effect of deformation microstructure on the GBCD optimization, and on the evolution of GBCD during TMP to explore the GBCD optimization mechanism; on that basis, whether IGSCC resistance in the high-nitrogen nickel-free ASS can be improved by GBCD optimization will be testified, and it is thus expected to provide a new solution to the problem of IGSCC caused by precipitation of nitrides during welding in the steel.

2 Experimental

The experimental steel Fe–18Cr–17Mn–2Mo–0.85N (wt%) used in the present study was melted by induction furnace and electroslag remelting (ESR) furnace both filled with N_2 and cast into water-cooled mold. After forging at 1473 K, the cast ingot was hot-rolled at 1373 K into a plate with 6 mm

thickness and then cold-rolled into plates with 4 mm thickness. The chemical composition of the experimental steel is listed in Table 1. The cold-rolled plates were heated at 1323 K for 1 h followed by water quenching (thereafter referred to as solid solution treatment). The solution-treated specimen was termed here as the base material (BM). The BM was cold-rolled by 5%, 7% and 10% in thickness reduction and then annealed at 1223 K and 1423 K for 10 min–72 h in vacuum and quickly cooled in water. For the electron backscatter diffraction (EBSD) measurements, the specimen surfaces were subsequently electropolished in a solution of $HClO_4$/$CH_3CH_2OH = 8:100$ (volume fraction) under 30 V for 15 s. The GBCD of specimen was examined by an orientation imaging microscopy (OIM) system, which is attached to a JEOL JSM 7001F field emission scanning electron microscope (FESEM). EBSD analyses were performed on at least four different areas (each 817×612 μm^2) for each specimen, with a step size of 1 μm. The fractions of the different grain boundary types were determined on the basis of the length fraction by dividing the number of pixels of a particular boundary by that of the entire grain boundaries. Grain boundaries with $\sum \leq 29$ were regarded as the low-energy CSL boundaries [4, 6], and the others are high-energy random boundaries. The Brandon criterion was used to assess the CSL boundaries [35]. The cold-rolled microstructures at different deformation amounts were observed by an FEI Tecnai G^2 20 transmission electron microscope (TEM). For quasi-in situ observations, the microstructures after cold-rolling and annealing were examined by EBSD measurements and the observed position was recorded and fixed using the ruler tool in SEM. Then, the specimens were continuously annealed for different times. Subsequently, the EBSD observation was performed again on the same region. Finally, the last two steps were repeated to complete quasi-in situ observations.

To explore the sensitization treatment process, BM and GBE specimens were sensitization-treated at 1123 K for 1 h and 2 h and then water-quenched to induce the precipitates at GBs. The IGSCC properties of BM and GBE specimens after sensitization treatments were evaluated by using MF DL100 slow strain rate testing (SSRT) machine. A strain rate of 1.0×10^{-5} s^{-1} and a solution (pH 2.6–2.8) of 5% NaCl + 0.5% acetic acid + deionized water (NACE/A solution) were adopted for the test. The test temperature was about 323K. The microstructures of specimens after SSRT were observed and analyzed by FESEM.

Table 1 Chemical composition of the experimental steel (wt%)

Cr	Mn	Mo	N	C	S	P	Al	Fe
18.36	16.52	2.32	0.85	0.023	0.0013	0.0041	0.0008	Bal.

3 Results and Discussion

3.1 Microstructure of BM Specimen

Figure 1 shows the inverse pole figure and the EBSD-reconstructed images in the BM. From Fig. 1, it can be seen that the microstructure of BM is mainly composed of equiaxed and randomly oriented grains (Fig. 1a) and some twins are formed inside grains (Fig. 1b). Apparently, the network of general high-angle boundaries (GHABs) presents a rather high connectivity (Fig. 1c).

3.2 Exploration of GBE Process

Figure 2 shows the fractions of SBs (f_{SBs}) of the specimens annealed at 1423 K for 10 min (high temperature + short time) and 1223 K for 24 h (low temperature + long time) under different cold-rolling reductions. From Fig. 2, one can see that the higher f_{SBs} are both obtained by 5% cold-rolling reduction under these two TMP processes and the highest f_{SBs} does not exceed 80%.

In order to obtain a much higher f_{SBs}, the specimens are annealed, respectively, at 1423 K and 1223 K for a long time (72 h) after 5% cold-rolling reduction. Table 2 lists the proportions of various SBs for BM and all specimens after TMP treatments. The highest f_{SBs} reaches 82.85% in the specimen cold-rolled by 5% and then annealed at 1423 K for 72 h (high temperature + long time) under the experimental conditions.

3.3 Deformed Microstructure and Evolution of GBCD

In the traditional 304 and 316 ASSs, the highest f_{SBs} is generally obtained by annealing at high temperature for a short
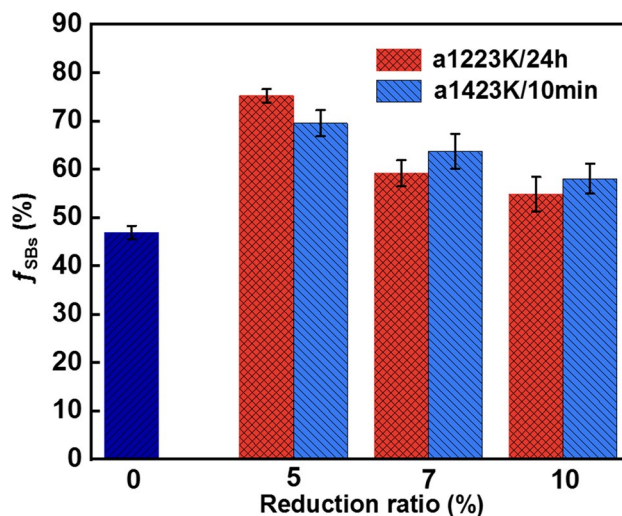

Fig. 2 Effect of cold-rolling reduction on the fraction of SBs in the high-nitrogen ASS

time or at low temperature for a long time after small pre-deformation, and detwinning may occur during the grain growth, resulting in a decrease in f_{SBs} [8, 10, 36]. However, the present study and our previous study [32] have ascertained that the highest f_{SBs} is obtained by annealing at high temperature for a long time after small pre-deformation in the Fe–Cr–Mn–Mo–N high-nitrogen ASS. Then, the relevant mechanism for the optimal TMP will be discussed from both deformation microstructures and heat treatment.

Deformation microstructures under different cold reductions are shown in Fig. 3. In the specimen with 5% reduction (Fig. 3a, b), the deformation microstructure is dominated by the stacking faults (SFs) and some planar slip bands. In addition, a few dipole arrays are also observed. As the reduction is 7%, SFs and planar slip bands are still the main
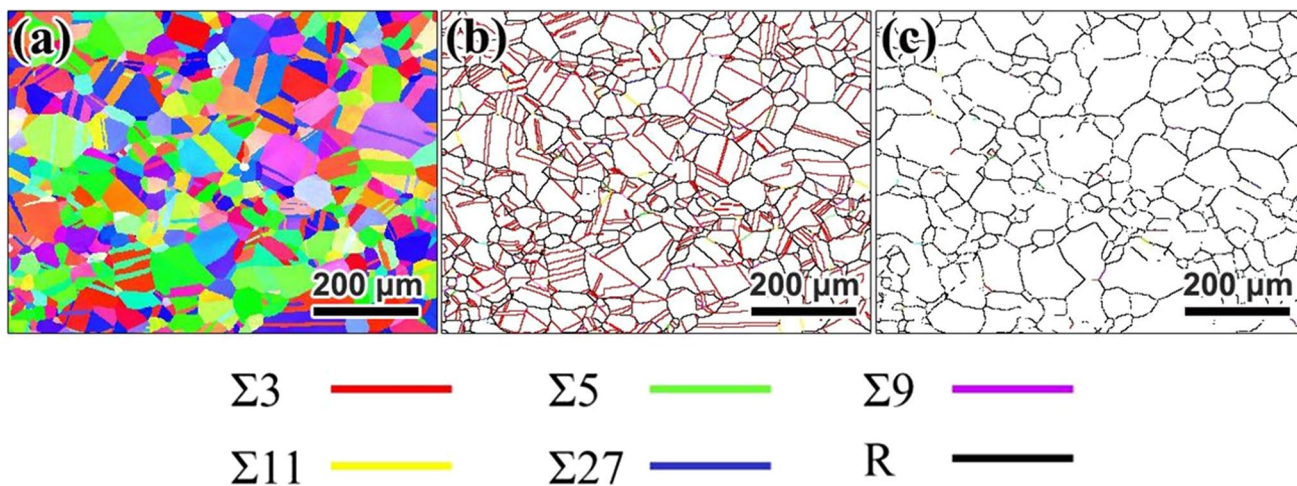

Fig. 1 Inverse pole figure **a**, GBCD **b** and corresponding GHABs network **c** map for BM

Table 2 Proportions of various SBs for the BM and specimens after different TMP treatments

Specimen	$\Sigma 3$ (%)	$\Sigma 9$ (%)	$\Sigma 27$ (%)	Other low CSL grain boundaries (%)	Total SBs (%)
BM	41.39	2.53	0.85	2.46	46.91
r5%-a1223K/24 h	61.71	7.27	4.68	1.54	75.20
r7%-a1223K/24 h	48.61	6.04	3.42	1.10	59.17
r10%-a1223K/24 h	45.71	4.03	2.43	2.67	54.84
r5%-a1423K/10 min	58.99	6.08	3.43	0.99	69.49
r7%-a1423K/10 min	53.72	6.00	2.66	1.32	63.70
r10%-a1423K/10 min	50.98	3.37	1.64	2.04	58.03
r5%-a1223K/72 h	51.60	4.31	1.94	0.79	58.64
r5%-a1423K/72 h	72.40	6.02	3.43	1.00	82.85

deformed microstructures, but double slips are greatly activated (Fig. 3c, d). As the reduction further increases to 10%, planar slip bands are still the main deformed microstructures, but deformation twins (DTs) rather than SFs are observed (Fig. 3e, f). As seen from Table 2, the f_{SBs} in the specimens with 10% cold reduction is lowest, which is closely related to the appearance of DTs under this cold reduction. Our previous investigations have reported that both SFs and planar slip bands can induce the formation of annealing twin (AT) during the subsequent annealing process in Cu–16at%Al alloy [36] and AL6XN super ASS [37]; however, on the contrary, DTs would greatly hinder the formation of ATs in the above two alloys [36, 37]. A similar phenomenon is also observed in the present high-nitrogen ASS with low SFE, namely, the appearance of a large number of SFs and some planar slip bands in the specimen with 5% reduction brings about the highest f_{SBs} during the subsequent annealing (Table 2).

In order to further explore the increase in f_{SBs} during recrystallization and grain growth, the quasi-in situ EBSD observation was performed in the specimens annealed at 1423 K for different times after 5% cold reduction, and the result is presented in Fig. 4. After annealing at 1423 K for 3 min, the microstructure (Fig. 4b) is still similar to the cold-rolled microstructure (Fig. 4a). After annealing for 6 min, recrystallization begins to occur (Fig. 4c) and nearly completes at 10 min (Fig. 4d). From Fig. 4, it can be seen that as the annealing time increases, the appearance of a large number of SBs interrupts the connectivity of GHABs. In particular, as shown by the arrows in Fig. 4d" and e", the growth of grain cluster, i.e., twin-related domain (TRD), can be observed at the stage of grain growth. As the annealing time increases, the TRD size continues to grow (Fig. 4f"). In addition to the f_{SBs}, the TRD size and the ratio of TRD size to grain size (ν) are also important indicators for GBCD optimization. The ratio ν implies the induced degree of multiple twinning during the evolution of TRD. Figures 5 and 6 show the effects of annealing times at 1423 K after 5% cold rolling on the f_{SBs} and $f_{\Sigma 3}$, TRD size and ν, respectively.

Clearly, as the annealing time increases, f_{SBs}, $f_{\Sigma 3}$, TRD size and ν all keep increasing and reach the maximum after annealing for 72 h. Accordingly, a conclusion can be drawn that the TRD size has been growing in the stage of grain growth under such a TMP (cold-rolled by 5% + annealed at 1423 K for 72 h).

The TRD, also called grain cluster, is referred to such a grain encircled by the GHABs, and a large amount of ΣCSL boundaries are contained within the grain [19, 33, 38–40]. It has been recognized that the f_{SBs} increases gradually accompanying with the growth of TRD during GBCD optimization [38–40]. SBs are mainly composed of $\Sigma 3$, $\Sigma 9$ and $\Sigma 27$ boundaries, among which the $\Sigma 3$ boundary (AT boundary) accounts for a larger proportion (Table 2). Therefore, the increase in f_{SBs} is mainly due to the increase in AT. Maximizing the number of ATs in the face-centered cubic metals is exactly the basis to achieve GBCD optimization. Based on the deformed microstructure and the quasi-in situ EBSD observations in Fe–Cr–Mn–Mo–N high-nitrogen ASS, it is recognized that, as with other ASSs, the growth of TRD during recrystallization is achieved by strain-driven migration of GHABs. ATs tend to form at the trailing edge of the migrating GHABs when SFs and planar slip bands in the pre-deformation (cold-rolled) microstructures encounter migrating GHABs. However, the DTs in pre-deformation microstructures are detrimental to the growth of TRD, thus impairing GBCD optimization [36, 37]. Therefore, the optimal pre-deformation to achieve the GBCD optimization should be slightly lower than the critical deformation amount of 10%, at which DTs start to nucleate. In addition, if the cold-rolling deformation is larger, the recrystallized grain will be finer; it is not conducive to the growth of TRD. To sum up, in the experimental steel, 5% is the most suitable cold-rolling deformation amount.

In the traditional ASS, it is considered that the increase in f_{SBs} is generally in the recrystallization stage [41], and therefore, annealing at high temperature for a short time or at low temperature for a long time after small pre-deformation is the optimal TMP. In particular, during the stage of grain
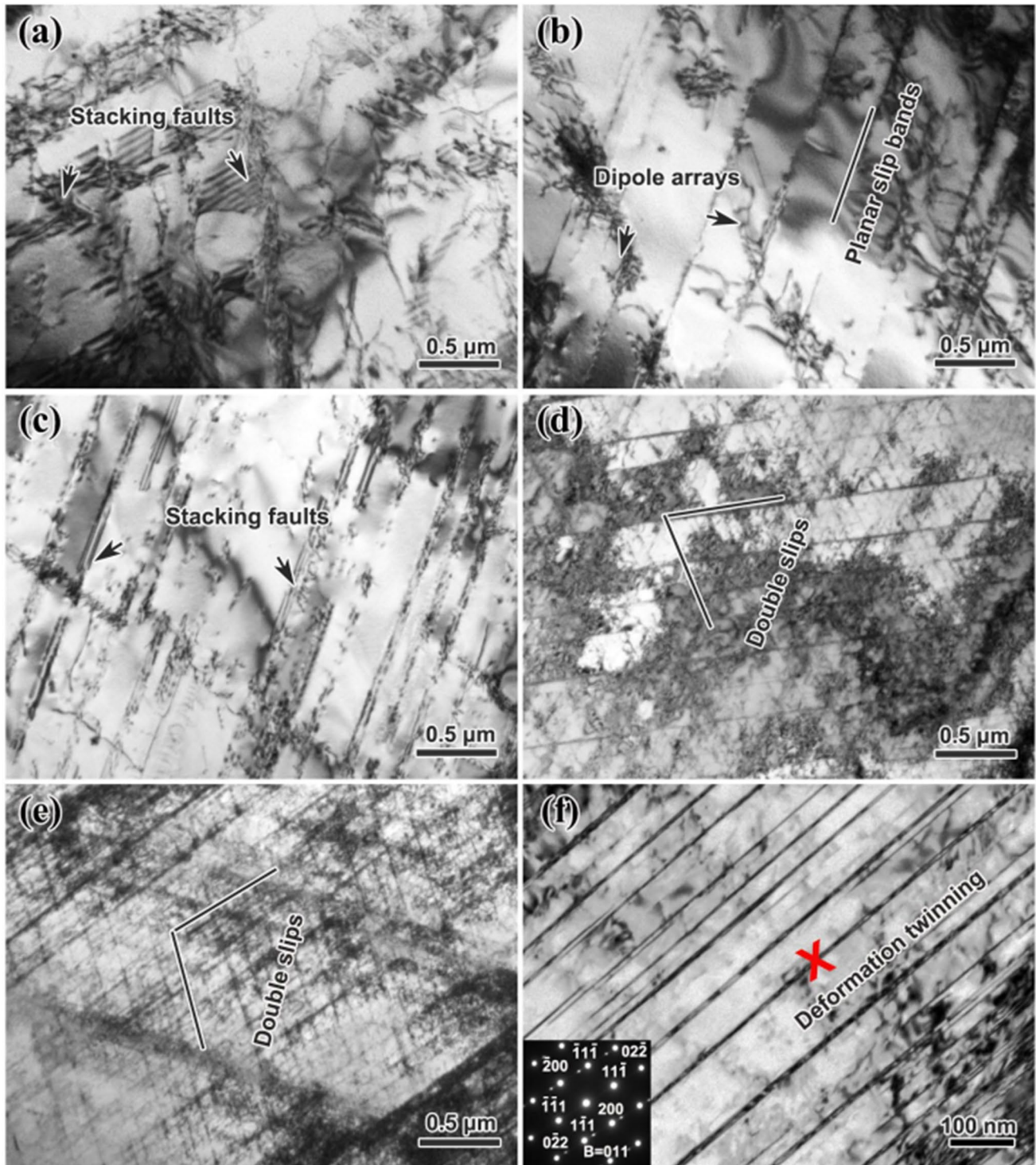
Fig. 3 TEM micrographs showing the evolution of deformation microstructures in the high-nitrogen ASS cold-rolled by 5% **a**, **b**, 7% **c**, **d** and 10% **e**, **f** reduction, respectively

growth, TRD has also been growing in Fe–Cr–Mn–Mo–N high-nitrogen ASS (Figs. 4, 6). However, the growth of TRD during grain growth is achieved by interface-driven migration of GHABs. The impingement of two small TRDs can form SBs with prolonging annealing time and increase the TRD size (Fig. 4d", e"). Therefore, the TRD size is an important sign of GBCD optimization. The acquisition of a high proportion of SBs actually includes the formation
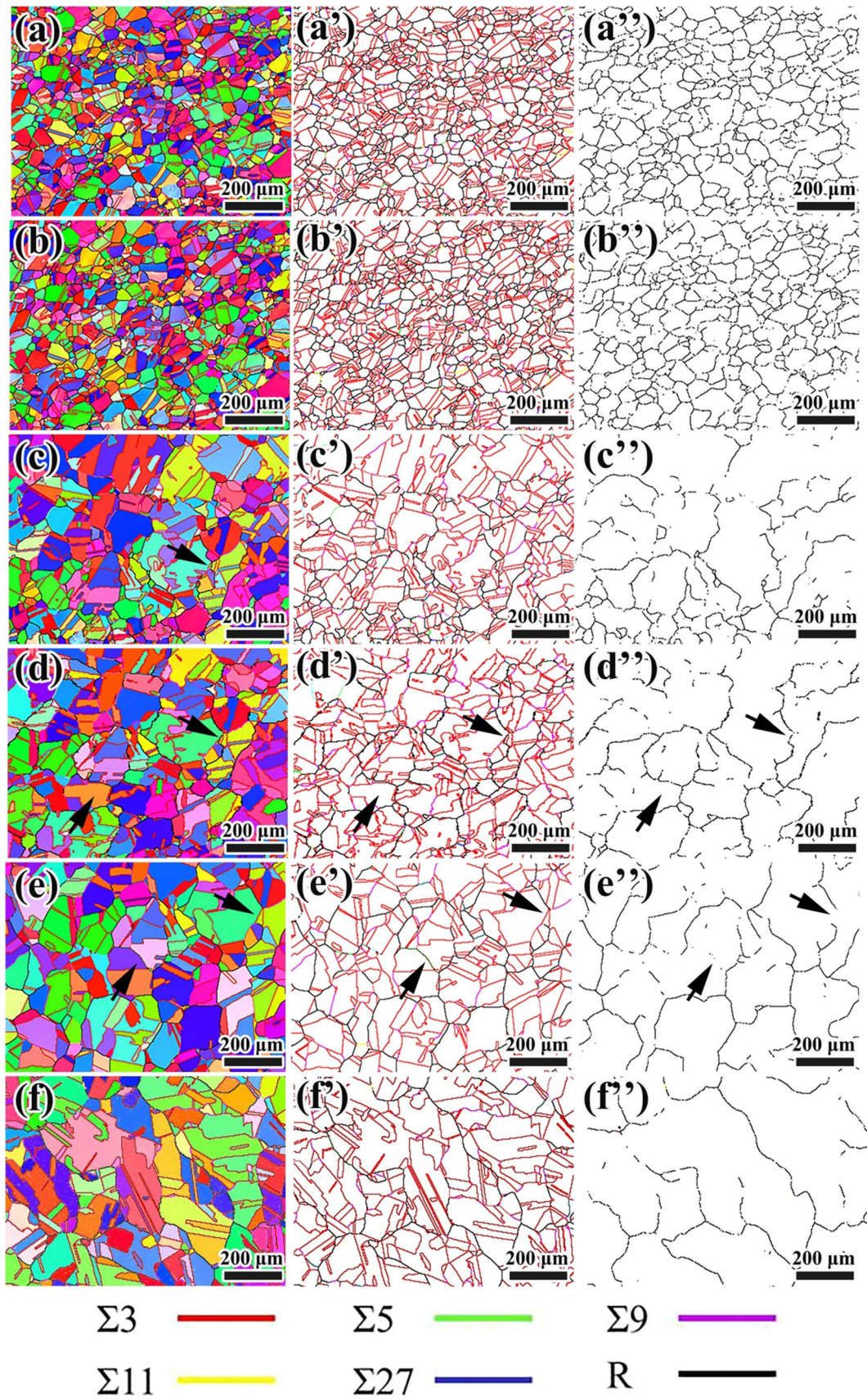
$\Sigma 3$ —— $\Sigma 5$ —— $\Sigma 9$ ——

$\Sigma 11$ —— $\Sigma 27$ ——   R ——

of ATs during recrystallization and SBs created by the impingement of the growing TRD during grain growth in the experimental steel. Therefore, f_{SBs} continues to increase with the increase in TRD size and the large-sized TRD becomes a common feature of the microstructure after GBCD optimization [7, 33, 42]. The ν value can reflect TRD evolution and the induction degree of ATs. Therefore, the larger the TRD size and ν value are, the higher the f_{SBs} is, and the GBCD is better optimized.

As stated above, 5% cold deformation provides a suitable deformation structure for the subsequent heat treatment. Higher annealing temperature favors the migration of GHABs during annealing stage, and the increase in annealing time induces impingement of two small TRDs during grain growth stage, which leads to the growth of TRD and the increase in f_{SBs}. Therefore, GBCD of the experimental steel has been well optimized under such a TMP condition, i.e., cold-rolled by 5% + annealed at 1423 K for 72 h.

3.4 Effect of GBCD Optimization on the IGSCC Behavior

To clarify the relationship between GBCD optimization and IGSCC resistance in the experimental steel, the BM with the lowest f_{SBs} (47.23%) and the r5%-a1423K/72 h specimen with the highest f_{SBs} (82.85%) are chosen for IGSCC performance tests. Figure 7 shows the optical microstructures of these two specimens after sensitization treatments. According to our previous studies [29, 33, 43], the granular precipitates at GBs and cellular ones toward grain interiors indicated by the arrows are all Cr_2N precipitates. Table 3 lists the fractions of precipitates for the BM and r5%-a1423K/72 h specimens sensitized at 1123 K for different times.

Several studies [44, 45] have shown that the carbides have a high tendency to precipitate at the GHABs rather than low-ΣCSL boundaries. From Fig. 7 and Table 3, it can be seen that the fraction of Cr_2N precipitates increases with increasing aging time. However, regardless of the aging time, the fraction of precipitates in the GBE specimen is always less than that of the BM. This is due to the fact that SBs have a lower interfacial energy compared with GHABs [4, 6]. GBE specimen contains a large number of SBs (Table 2), thus inhibiting the precipitation behavior at the GBs. The difference in precipitation behavior must have a certain impact on the IGSCC performance of BM and GBE specimens. Since the suppression effect of annealing at 1123 K for 2 h is more obvious, it is selected as the sensitization treatment system before IGSCC performance testing of the experimental steel.

Figure 8 shows the stress–strain curves for the BM and r5%-a1423K/72 h specimens at a strain rate of 10^{-5} s^{-1} in a NACE/A solution at 323 K after sensitized at 1123 K for 2 h. To analyze more clearly the effect of GBCD optimization on the IGSCC performance, the specific data are listed in Table 4. Apparently, after tensioning at a slow strain rate, there is a slight decrease in tensile strength but an obvious improvement in elongation for the GBE specimen compared with the BM. Rupture time is an important parameter describing the sensitivity of IGSCC. The rupture times t_f of the BM and r5%-a1423K/72 h specimens are, respectively, 14.8 h and 18.3 h. The rupture time of r5%-a1423K/72 h specimen is extended by 23.6% compared with that of the BM, indicating that the IGSCC resistance is improved after such a GBE treatment.

Figure 9 shows the deformation and damage characteristics on the fracture surface of the BM and r5%-a1423K/72 h specimens after slow strain rate stretching. From Fig. 9a, it can be seen that those cracks are basically large-sized intergranular cracks along GHABs in the BM; however, such large-sized intergranular cracks are greatly inhibited in the r5%-a1423K/72 h specimen, except that a few small-sized intergranular cracks and some transgranular cracks are observed (Fig. 9b).

Figure 10 shows the microstructures near fracture zones of the BM and r5%-a1423K/72 h specimens after SSRT. From Fig. 10a, it can be observed that the GB corrosion is very serious, and the corrosion grooves at the GBs are rather deep and wide and some grains have been dropped in the BM. However, in the GBE specimen (Fig. 10b), the corrosion grooves of GBs are not connected and the degree of GB corrosion becomes significantly weakened compared with the case of the BM.

The connectivity of the grain boundary network can be quantitatively described through measuring triple junction (TJ) distributions [15]. TJs can be divided into four types: $J0$ (0-CSL), $J1$ (1-CSL), $J2$ (2-CSL) and $J3$ (3-CSL). The effect of GBCD optimization can be reflected from the ratio of the four kinds of TJs. EBSD characterizations (Fig. 11) demonstrate that both ends of the intergranular crack are arrested at $J2$ type of TJs in the GBE specimen, as indicated by the arrows in Fig. 11b. The other case is that both ends of the intergranular crack are arrested, respectively, at $J2$ type and $J3$ type of TJs, as shown by the arrows in Fig. 11d.

In addition to intergranular cracks, transgranular cracks are also observed in the GBE specimen (Fig. 9b). There are a large number of SBs and $J3$ type of TJs such as Σ3–Σ3–Σ9 and Σ3–Σ9–Σ27 inside the grain with GHABs. When the transgranular crack propagates to encounter SBs and $J3$ type of TJs, the propagation direction would change and the crack tip energy is thus successively decreased, so that the crack propagation is arrested. Figure 12 shows the change in the
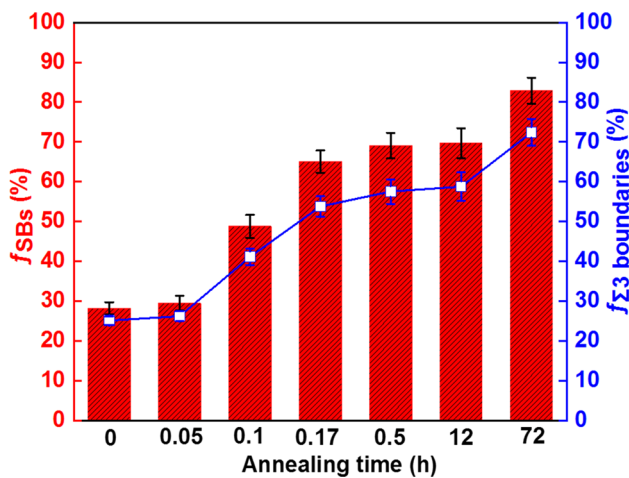
Fig. 5 Effects of annealing at 1423 K for different time after cold-rolled by 5% on the fractions of SBs and $\Sigma3$ boundaries in the high-nitrogen ASS
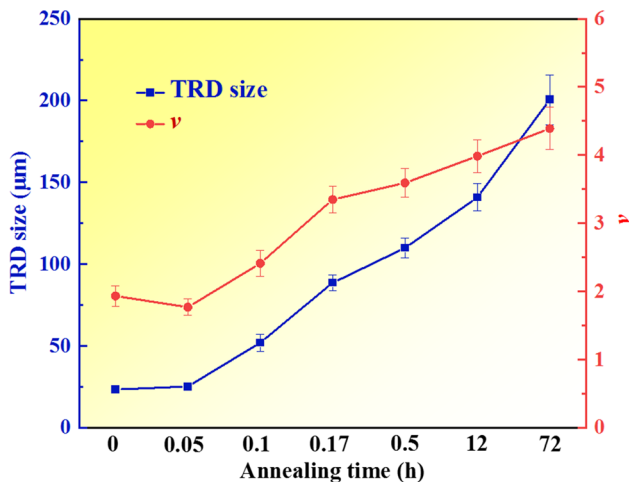

Fig. 6 Effects of annealing at 1423 K for different time after cold-rolled by 5% on the TRD size and ν value in the high-nitrogen ASS

propagation direction of a transgranular crack, and it finally terminates inside the grain with GHABs in the GBE specimen.

Figure 13a shows TJ fractions for BM and r5%-a1423K/72 h specimens. It can be seen that the fractions of $J2$ and $J3$ increase, whereas the fractions of $J0$ and $J1$ decrease after GBCD optimization.

Some investigators have proposed the crack arrest probability P on the basis of TJs and f_{SBs} [4, 46]. For example, Kumar et al. [15, 46] reported that the percolative paths in the microstructure would be broken if the following inequality holds:

$$P_K = J2/(1 - J3) \geq 0.35. \tag{1}$$

where P_K reflects the connectivity of GHABs. When P_K is greater than or equal to 0.35, the connectivity of GHABs network would be generally well blocked and the percolative paths would be broken [46, 47].

The above crack arrest probability is calculated from the type of TJs. Considering the contribution of f_{SBs}, Palumbo [4] proposed the other model to calculate the crack arrest probability, as expressed by

$$P_P = (f_{SBs}^2) + 2[(f_0)(f_{SBs})(1 - f_{SBs})]. \tag{2}$$

where f_{SBs} is the fraction of SBs and f_0 is the fraction of interfaces in the distribution that are unfavorably oriented to the stress axis.

Probabilities for crack arrest of BM and r5%-a1423K/72 h specimens are calculated according to the above two models, and the result is presented in Fig. 13b. It can be found that probabilities for crack arrest calculated by two methods are both higher in GBE specimen than those in BM and the P_K of r5%-a1423K/72 h specimen is 0.36 (> 0.35), while the P_K of BM is only 0.17 (< 0.35), which indicates that the connectivity of GHABs network is generally well blocked and the percolative paths are broken in the GBE specimen, thus further convincingly confirming that a GBE treatment can improve the IGSCC resistance of the experimental steel.

IGSCC susceptibility is correlated with the degree of sensitization in sensitized ASSs [48]. Degree of sensitization largely depends on the formation of Cr-depleted regions along the GBs. The appearance of the Cr-depleted zone near the GBs is related to the Cr precipitation at the GBs. Studies by Toppo et al. [48] have shown that, as the N content reached 0.22% in 316LN ASS, the IGSCC susceptibility increased significantly due to the precipitation of $Cr_{23}C_6$ and Cr_2N. The nitrogen content of the experimental steel is very high (0.85 mass%); after a sensitization treatment, in the BM, a large number of Cr_2N precipitates at GBs lead to Cr depletion near the GBs and weaken GBs, that is to say, the number of susceptible GBs becomes larger. Lots of intergranular cracks are thus observed in the fracture surface (Fig. 9a), and GB corrosion is very serious in the near fracture zone (Fig. 10a). Therefore, it can be seen that the experimental steel has a very large susceptibility to IGSCC under the combined actions of tensile stress at the strain rate 10^{-5} s^{-1} and acidic Cl$^-$ solution. After a GBCD optimization, the appearance of a large number of SBs (Table 2) suppresses the second-phase precipitation (Table 3), interrupts the connectivity of non-corrosion-resisting boundaries network, reduces the susceptibility to GB corrosion (Fig. 10b) and thus weakens GB cracking, and also increases the special TJs (such as $J2$ or $J3$), which arrests intergranular cracks (Fig. 11).
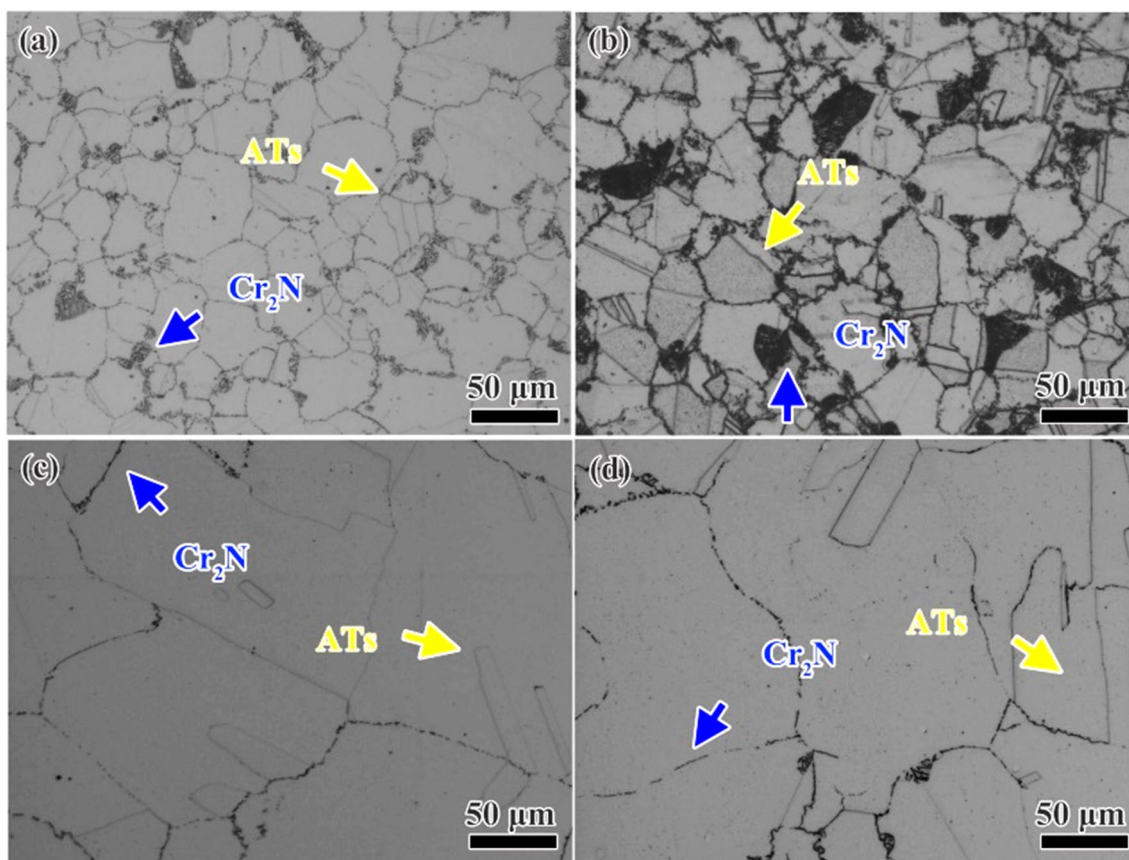
Fig. 7 Optical micrographs of the BM **a**, **b** and r5%-a1423K/72 h **c**, **d** specimens sensitized at 1123 K for different time of 1 h **a**, **c** and 2 h **b**, **d**

Table 3 Fraction of precipitates for the BM and r5%-a1423K/72 h specimens sensitized at 1123 K for different time

Specimen	Fraction of precipitates (%) for 1 h	Fraction of precipitates (%) for 2 h
BM	3.1 ± 0.4	8.5 ± 0.7
r5%-a1423K/72 h	0.2 ± 0.05	0.4 ± 0.08

In a word, an appropriate TMP can induce a high f_{SBs}, large-sized TRDs and special TJs of high proportion, which makes the GBCD of the experimental steel well optimized. The appearance of low-energy SBs of high proportion suppresses the precipitation of intergranular nitrides and reduces the susceptibility to GB corrosion, and the special TJs of high proportion ($J2$, $J3$) prevent the intergranular propagation of cracks, thereby improving the IGSCC resistance of high-nitrogen ASS.
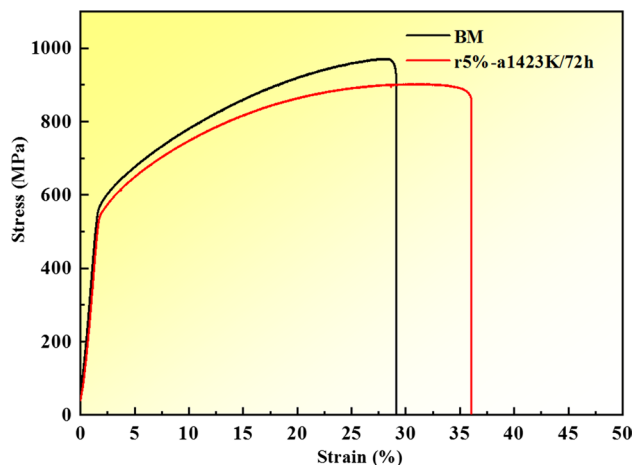

Fig. 8 Stress–strain curves for the BM and r5%-a1423K/72 h specimens in a NACE/A solution at 323 K after sensitized at 1123 K for 2 h

Table 4 Experimental data of the BM and r5%-a1423K/72 h specimens after SSRT

Specimen	t_f (h)	σ_f (MPa)	δ_f (%)
BM	14.8	970.9	29.13
r5%-a1423K/72 h	18.3	902	36.05

right amount of deformation (lower than 10%) are beneficial to the GBCD optimization.

2. SBs and special TJs ($J2$, $J3$) of high proportion hinder the second-phase precipitation along GBs and prevent the intergranular propagation of cracks, and thus improve the IGSCC resistance of the experimental steel.
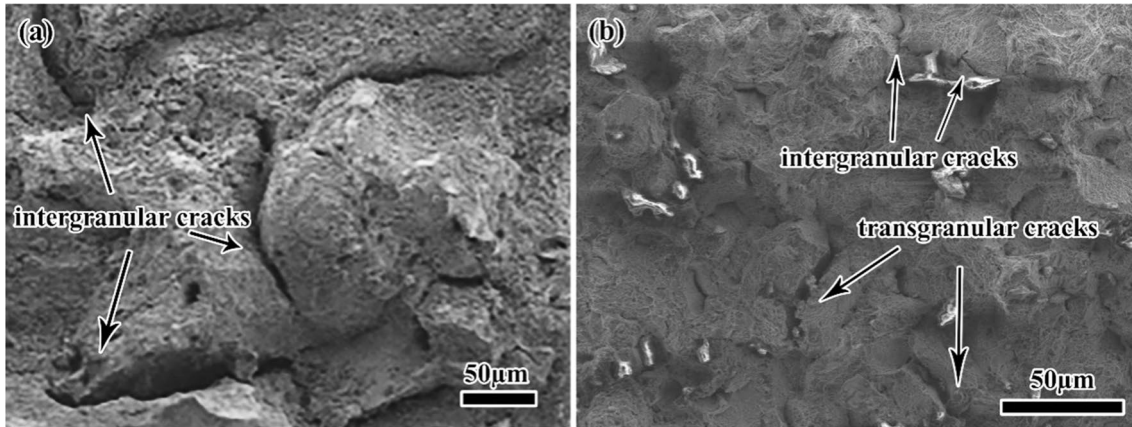
4 Conclusions

1. In the experimental steel Fe–18Cr–17Mn–2Mo–0.85N, the fraction of low ΣCSL boundaries increases from 46.91% for the solid solution-treated specimen to 82.85% for the specimen cold-rolled by 5% and then annealed at 1423 K for 72 h. Deformation microstructures, like SFs and planar slip bands, appearing at the

Fig. 9 SEM micrographs showing the fracture surfaces for BM **a** and r5%-a1423K/72 h **b** specimens after SSRT in a NACE/A solution environment
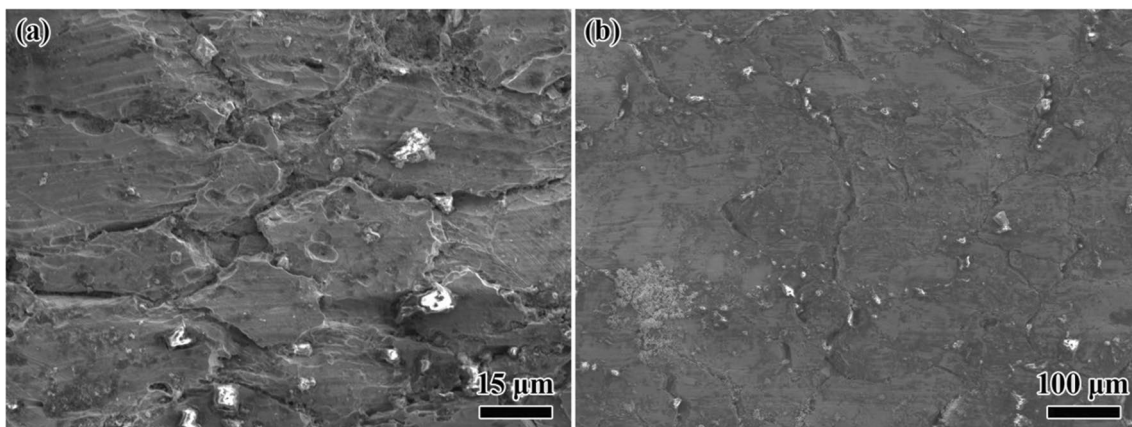

Fig. 10 SEM micrographs showing the microstructures in the near fracture zone for BM **a** and r5%-a1423K/72 h **b** specimens after SSRT in a NACE/A solution environment
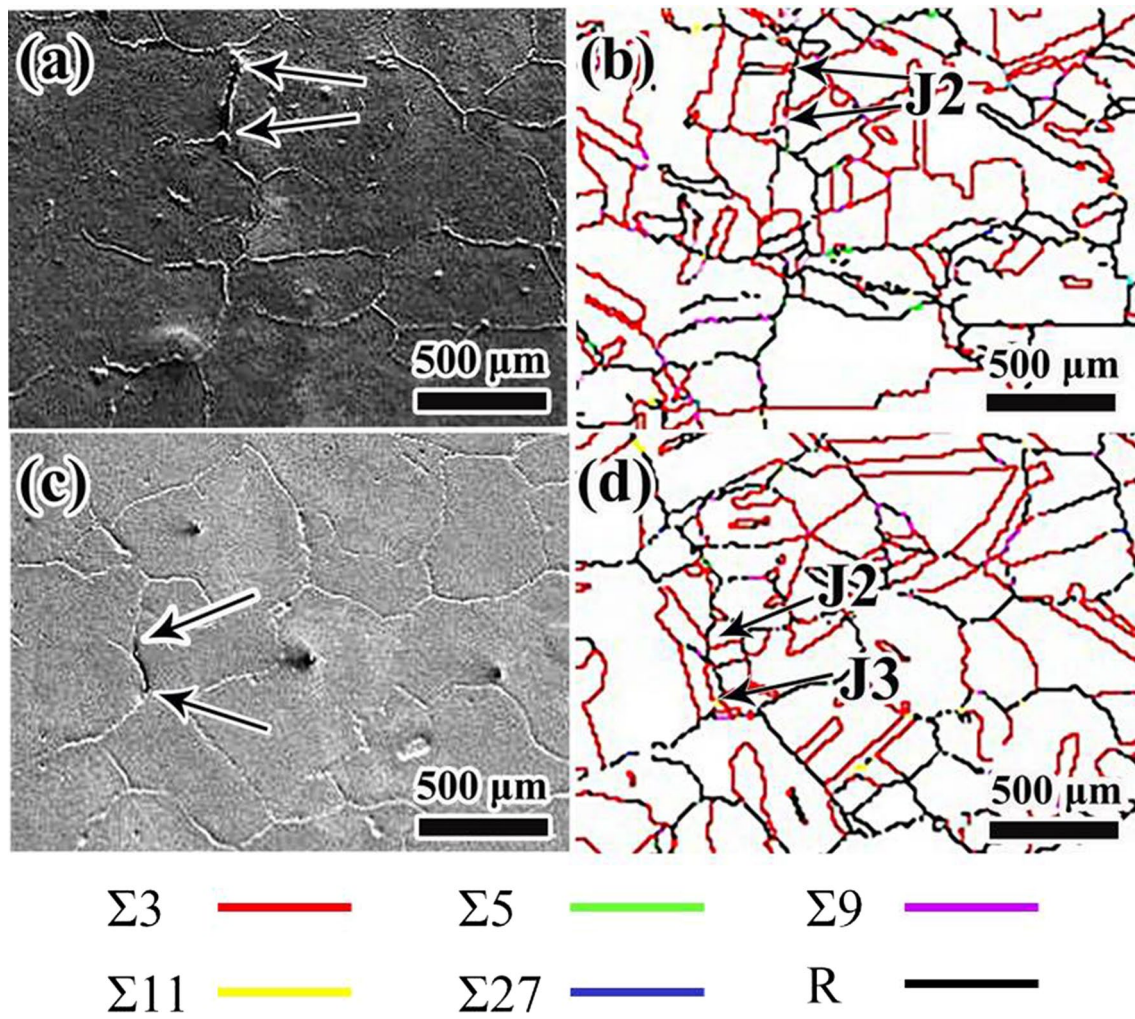
Fig. 11 Analysis of intergranular cracks under IGSCC tests in the GBCD-optimized high-nitrogen ASS: **a**, **c** fore scattered detector (FSD); **b**, **d** corresponding grain boundary map
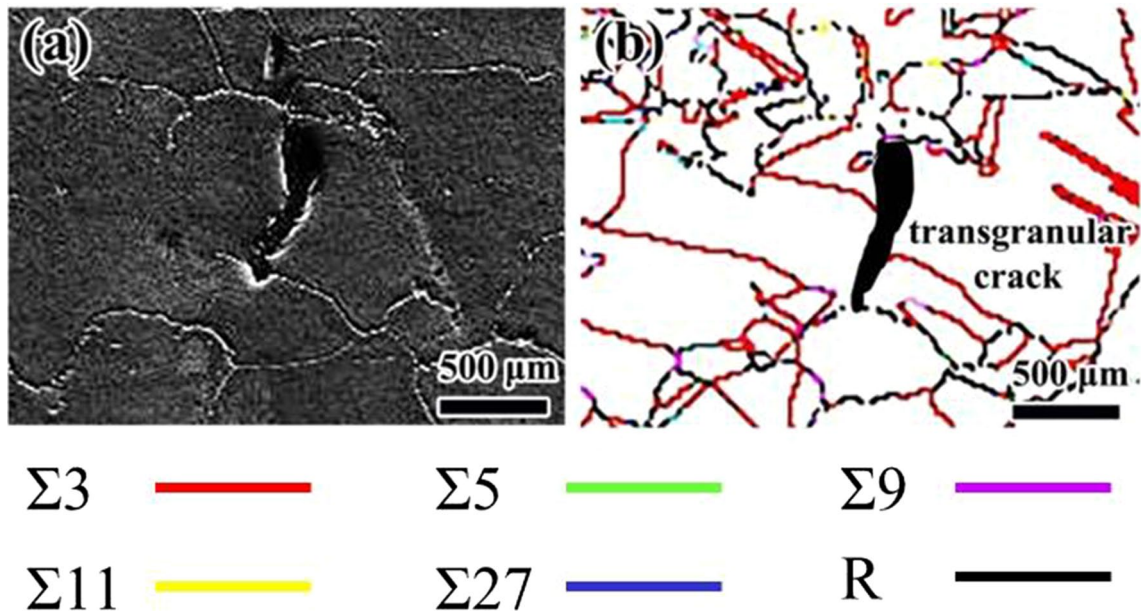
Fig. 12 Analysis of a transgranular crack under IGSCC tests in the GBCD-optimized high-nitrogen ASS: **a** fore scattered detector (FSD); **b** corresponding grain boundary map
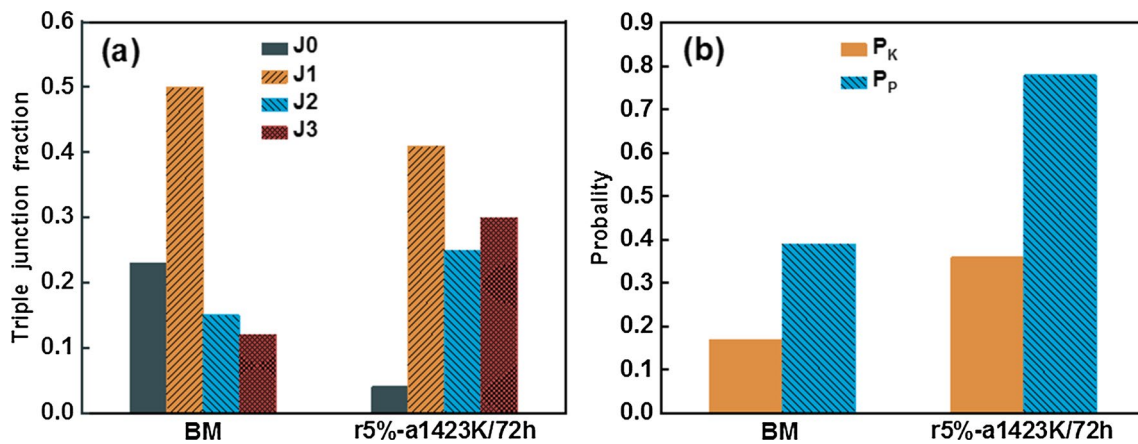

Fig. 13 Comparisons of the TJ fraction **a** and the probability for crack arrest **b** proposed by Kumar et al. [38] and Palumbo et al. [4] between the BM and r5%-a1423K/72 h specimens

References

[1] J. Gao, J.B. Tan, X.Q. Wu, S. Xia, Corros. Sci. **152**, 190 (2019)
[2] T. Watanabe, J. Mater. Sci. **46**, 4095 (2011)
[3] K. Deepak, S. Mandal, C.N. Athreya, D.I. Kim, B.D. Boer, V.S. Sarma, Corros. Sci. **106**, 293 (2016)
[4] G. Palumbo, P.J. King, K.T. Aust, U. Erb, P.C. Lichtenberger, Scr. Metall. Mater. **25**, 1775 (1991)
[5] T. Watanabe, S. Tsurekawa, Mater. Sci. Eng. A **387**, 447 (2004)
[6] T. Watanabe, Res. Mech. **11**, 47 (1984)
[7] C.L. Hu, S. Xia, H. Li, T.G. Liu, B.X. Zhou, W.J. Chen, N. Wang, Corros. Sci. **53**, 1880 (2011)
[8] M. Shimada, H. Kokawa, Z.J. Wang, Y.S. Sato, I. Karibe, Acta Mater. **50**, 2331 (2002)
[9] H. Kokawa, M. Shimada, M. Michiuchi, Z.J. Wang, Y.S. Sato, Acta Mater. **55**, 5401 (2007)
[10] M. Michiuchi, H. Kokawa, Z.J. Wang, Y.S. Sato, K. Sakai, Acta Mater. **54**, 5179 (2006)
[11] E.A. West, G.S. Was, J. Nucl. Mater. **392**, 264 (2009)

[12] T.G. Liu, S. Xia, Q. Bai, B.X. Zhou, L.F. Zhang, Y.H. Lu, T. Shoji, J. Nucl. Mater. **498**, 290 (2018)
[13] T.G. Liu, S. Xia, D.H. Du, Q. Bai, L.F. Zhang, Y.H. Lu, Mater. Lett. **234**, 201 (2019)
[14] P. Lin, G. Palumbo, U. Erb, K.T. Aust, Scr. Mater. **33**, 1387 (1995)
[15] A. Telang, A.S. Gill, D. Tammana, X.S. Wen, M. Kumar, S. Teysseyre, S.R. Mannava, D. Qian, V.K. Vasudevan, Mater. Sci. Eng. A **648**, 280 (2015)
[16] E.M. Lehockey, A.M. Brennenstuhl, I. Thompson, Corros. Sci. **46**, 2383 (2004)
[17] V.Y. Gertsman, S.M. Bruemmer, Acta Mater. **49**, 1589 (2001)
[18] A. Telang, A.S. Gill, M. Kumar, S. Teysseyre, D. Qian, S.R. Mannava, V.K. Vasudevan, Acta Mater. **113**, 180 (2016)
[19] S. Xia, H. Li, T.G. Liu, B.X. Zhou, J. Nucl. Mater. **416**, 303 (2011)
[20] H.Y. Ha, T.H. Lee, C.S. Oh, S.J. Kim, Scr. Mater. **61**, 121 (2009)
[21] J.W. Simmons, Mater. Sci. Eng. A **207**, 159 (1996)
[22] Y.S. Yoon, H.Y. Ha, T.H. Lee, S. Kim, Corros. Sci. **80**, 28 (2014)
[23] H. Baba, T. Kodama, Y. Katada, Corros. Sci. **44**, 2393 (2002)
[24] I. Olefjord, L. Wegrelius, Corros. Sci. **38**, 1203 (1996)
[25] M.G. Pujar, U.K. Mudali, S.S. Singh, Corros. Sci. **53**, 4178 (2011)
[26] M. Metikoš-Huković, R. Babić, Z. Grubač, Ž Petrović, N. Lajci, Corros. Sci. **53**, 2176 (2011)
[27] H.B. Li, Z.H. Jiang, Z.R. Zhang, Y. Cao, Y. Yang, Int. J. Min. Met. Mater. **16**, 654 (2009)
[28] M. Ogawa, K. Hiraoka, Y. Katada, M. Sagara, S. Tsukamoto, ISIJ Int. **42**, 1391 (2002)
[29] F. Shi, L.J. Wang, W.F. Cui, C.M. Liu, J. Iron Steel Res. Int. **15**, 72 (2008)
[30] F. Shi, Y. Qi, C.M. Liu, J. Mater. Sci. Technol. **27**, 1125 (2011)
[31] H. Kokawa, W.Z. Jin, Z.J. Wang, M. Michiuchi, Y.S. Sato, W. Dong, Y. Katada, Mater. Sci. Forum **539**, 4962 (2007)
[32] F. Shi, R.H. Gao, X.J. Guan, C.M. Liu, X.W. Li, Acta Metall. Sin. -Engl. Lett. **33**, 789 (2020)
[33] F. Shi, P.C. Tian, N. Jia, Z.H. Ye, Y. Qi, C.M. Liu, X.W. Li, Corros. Sci. **107**, 49 (2016)
[34] F. Shi, X.W. Li, Y.T. Hu, C. Su, C.M. Liu, Acta Metall. Sin. -Engl. Lett. **26**, 497 (2013)
[35] D.G. Brandon, Acta Metall. **14**, 1479 (1966)
[36] X.J. Guan, F. Shi, H.M. Ji, X.W. Li, Mater. Sci. Eng. A **765**, 138299 (2019)
[37] X.J. Guan, F. Shi, Z.P. Jia, X.W. Li, Mater. Charact. **170**, 110689 (2020)
[38] S. Tokita, H. Kokawa, Y.S. Sato, H.T. Fujii, Mater. Charact. **131**, 31 (2017)
[39] V. Randle, Acta Metall. Mater. **42**, 1769 (1994)
[40] B.W. Reed, M. Kumar, Scr. Mater. **54**, 1029 (2006)
[41] B.R. Kumar, S.K. Das, B. Mahato, A. Das, S.G. Chowdhury, Mater. Sci. Eng. A **454–455**, 239 (2007)
[42] X.Y. Fang, W.G. Wang, Z.X. Cai, C.X. Qin, B.X. Zhou, Mater. Sci. Eng. A **527**, 1571 (2010)
[43] F. Shi, L.J. Wang, W.F. Cui, C.M. Liu, Acta Metall. Sin. -Engl. Lett. **20**, 95 (2007)
[44] H.U. Hong, B.S. Rho, S.W. Nam, Mater. Sci. Eng. A **318**, 285 (2001)
[45] M. Kurban, U. Erb, K.T. Aust, Scr. Mater. **54**, 1053 (2006)
[46] M. Kumar, W.E. King, A.J. Schwartz, Acta Mater. **48**, 2081 (2000)
[47] C.A. Schuh, M. Kumar, W.E. King, Acta Mater. **51**, 687 (2003)
[48] A. Toppo, V. Shankar, R.P. George, J. Philip, Corrosion **76**, 591 (2020)